

Pupil stabilization for SPHERE's extreme AO and high performance coronagraph system.

Guillaume Montagnier,^{1,3} Thierry Fusco,² Jean-Luc Beuzit,¹ David Mouillet,¹ Julien Charton,¹ and Laurent Jocou¹

¹LAOG: Laboratoire d'Astrophysique de Grenoble, BP 53,
F-38041 Grenoble Cedex 9, France

²ONERA, BP72, 29 avenue de la Division Leclerc,
F-92322 Chatillon Cedex, France

³Observatoire de Genève, 51 chemin des Maillettes,
1290 Sauverny, Switzerland

Guillaume.Montagnier@obs.ujf-grenoble.fr

Abstract: We propose a new concept of pupil motion sensor for astronomical adaptive optics systems and present experimental results obtained during the first laboratory validation of this concept. Pupil motion is an important issue in the case of extreme adaptive optics, high contrast systems, such as the proposed Planet Finder instruments for the ESO and Gemini 8-meter telescopes. Such high contrast imaging instruments will definitely require pupil stabilization to minimize the effect of quasi-static aberrations. The concept for pupil stabilization we propose uses the flux information from the AO system wave-front sensor to drive in closed loop a pupil tip-tilt mirror located in a focal plane. A laboratory experiment validates this concept and demonstrates its interest for high contrast imaging instrument.

© 2018 Optical Society of America

OCIS codes: 010.1080, 220.4830

References and links

1. G. Rousset, F. Lacombe, P. Puget, N. N. Hubin, E. Gendron, T. Fusco, R. Arsenault, J. Charton, P. Feautrier, P. Gigan, P. Y. Kern, A.-M. Lagrange, P.-Y. Madec, D. Mouillet, D. Rabaud, P. Rabou, E. Stadler, and G. Zins, "NAOS, the first AO system of the VLT: on-sky performance," in *Adaptive Optical System Technologies II. Edited by Wizinowich, Peter L.; Bonaccini, Domenico. Proceedings of the SPIE, Volume 4839, pp. 140-149 (2003).*, P. L. Wizinowich and D. Bonaccini, eds., vol. 4839 of *Presented at the Society of Photo-Optical Instrumentation Engineers (SPIE) Conference*, pp. 140–149 (2003).
2. J. A. Stoesz, J.-P. Veran, F. J. Rigaut, G. Herriot, L. Jolissaint, D. Frenette, J. Dunn, and M. Smith, "Evaluation of the on-sky performance of Altair," in *Advancements in Adaptive Optics. Edited by Domenico B. Calia, Brent L. Ellerbroek, and Roberto Ragazzoni. Proceedings of the SPIE, Volume 5490, pp. 67-78 (2004).*, D. Bonaccini Calia, B. L. Ellerbroek, and R. Ragazzoni, eds., vol. 5490 of *Presented at the Society of Photo-Optical Instrumentation Engineers (SPIE) Conference*, pp. 67–78 (2004).
3. P. L. Wizinowich, D. Le Mignant, A. H. Bouchez, R. D. Campbell, J. C. Y. Chin, A. R. Contos, M. A. van Dam, S. K. Hartman, E. M. Johansson, R. E. Lafon, H. Lewis, P. J. Stomski, D. M. Summers, C. G. Brown, P. M. Danforth, C. E. Max, and D. M. Pennington, "The W. M. Keck Observatory Laser Guide Star Adaptive Optics System: Overview," *PASP***118**, 297–309 (2006).

4. A. Boccaletti, P. Riaud, P. Baudoz, J. Baudrand, D. Rouan, D. Gratadour, F. Lacombe, and A.-M. Lagrange, "The Four-Quadrant Phase Mask Coronagraph. IV. First Light at the Very Large Telescope," *PASP***116**, 1061–1071 (2004).
5. G. Chauvin, A.-M. Lagrange, C. Dumas, B. Zuckerman, D. Mouillet, I. Song, J.-L. Beuzit, and P. Lowrance, "Giant planet companion to 2MASSW J1207334-393254," *A&A***438**, L25–L28 (2005). [arXiv:astro-ph/0504659](#).
6. G. Chauvin, A.-M. Lagrange, B. Zuckerman, C. Dumas, D. Mouillet, I. Song, J.-L. Beuzit, P. Lowrance, and M. S. Bessell, "A companion to AB Pic at the planet/brown dwarf boundary," *A&A***438**, L29–L32 (2005). [arXiv:astro-ph/0504658](#).
7. R. Neuhauser, E. W. Guenther, G. Wuchterl, M. Mugrauer, A. Bedalov, and P. H. Hauschildt, "Evidence for a co-moving sub-stellar companion of GQ Lup," *A&A***435**, L13–L16 (2005). [arXiv:astro-ph/0503691](#).
8. J.-L. Beuzit, M. Feldt, K. Dohlen, D. Mouillet, P. Puget, J. Antici, A. Baruffolo, P. Baudoz, A. Berton, A. Boccaletti, M. Carillet, J. Charton, R. Claudi, M. Downing, P. Feautrier, E. Fedrigo, T. Fusco, R. Gratton, N. Hubin, M. Kasper, M. Langlois, C. Moutou, L. Mugnier, J. Pragt, P. Rabou, M. Saisse, H. M. Schmid, E. Stadler, M. Turatto, S. Udry, R. Waters, and F. Wildi, "SPHERE: A 'Planet Finder' Instrument for the VLT," *The Messenger* **125**, 29–+ (2006).
9. K. Dohlen, J.-L. Beuzit, M. Feldt, D. Mouillet, P. Puget, J. Antichi, A. Baruffolo, P. Baudoz, A. Berton, A. Boccaletti, M. Carillet, J. Charton, R. Claudi, M. Downing, C. Fabron, P. Feautrier, E. Fedrigo, T. Fusco, J.-L. Gach, R. Gratton, N. Hubin, M. Kasper, M. Langlois, A. Longmore, C. Moutou, C. Petit, J. Pragt, P. Rabou, G. Rousset, M. Saisse, H.-M. Schmid, E. Stadler, D. Stamm, M. Turatto, R. Waters, and F. Wildi, "SPHERE: A planet finder instrument for the VLT," in *Ground-based and Airborne Instrumentation for Astronomy. Edited by McLean, Ian S.; Iye, Masanori. Proceedings of the SPIE, Volume 6269, pp. 62690Q (2006).*, vol. 6269 of *Presented at the Society of Photo-Optical Instrumentation Engineers (SPIE) Conference* (2006).
10. T. Fusco, C. Petit, G. Rousset, J.-F. Sauvage, K. Dohlen, D. Mouillet, J. Charton, P. Baudoz, M. Kasper, E. Fedrigo, P. Rabou, P. Feautrier, M. Downing, P. Gigan, J.-M. Conan, J.-L. Beuzit, N. Hubin, F. Wildi, and P. Puget, "Design of the extreme AO system for SPHERE, the planet finder instrument of the VLT," in *Advances in Adaptive Optics II. Edited by Ellerbroek, Brent L.; Bonaccini Calia, Domenico. Proceedings of the SPIE, Volume 6272, pp. 62720K (2006).*, vol. 6272 of *Presented at the Society of Photo-Optical Instrumentation Engineers (SPIE) Conference* (2006).
11. R. Racine, G. A. H. Walker, D. Nadeau, R. Doyon, and C. Marois, "Speckle Noise and the Detection of Faint Companions," *PASP***111**, 587–594 (1999).
12. A. Berton, R. G. Gratton, M. Feldt, T. Henning, S. Desidera, M. Turatto, H. M. Schmid, and R. Waters, "Detecting Extrasolar Planets with Integral Field Spectroscopy," *PASP***118**, 1144–1164 (2006). [arXiv:astro-ph/0605207](#).
13. H. M. Schmid, D. Gisler, F. Joos, H. P. Povel, J. O. Stenflo, M. Feldt, R. Lenzen, W. Brandner, J. Tinbergen, A. Quirrenbach, R. Stuik, R. Gratton, M. Turatto, and R. Neuhauser, "ZIMPOL/CHEOPS: a Polarimetric Imager for the Direct Detection of Extra-solar Planets," in *Astronomical Polarimetry: Current Status and Future Directions*, A. Adamson, C. Aspin, C. Davis, and T. Fujiyoshi, eds., vol. 343 of *Astronomical Society of the Pacific Conference Series*, pp. 89–+ (2005).
14. S. F. Clifford, "The Classical Theory of Wave Propagation in a Turbulent Medium," in *Laser Beam Propagation in the Atmosphere. Edited by J. W. Strohbehn, Springer Verlag, Berlin Heidelberg New York, pp. 9-41 (1978)*.
15. F. Roddier, "The effects of atmospheric turbulence in optical astronomy," in *Progress in optics. Volume 19. Amsterdam, North-Holland Publishing Co., 1981, p. 281-376.*, vol. 19, pp. 281–376 (1981).
16. T. Fusco and J.-M. Conan, "On- and off-axis statistical behavior of adaptive-optics-corrected short-exposure Strehl ratio," *Journal of the Optical Society of America A* **21**, 1277–1289 (2004).
17. L. A. Poyneer and B. Macintosh, "Spatially filtered wave-front sensor for high-order adaptive optics," *J. Opt. Soc. Am. A* **21**, 810–819 (2004).
18. T. Fusco, C. Petit, G. Rousset, J.-M. Conan, and J.-L. Beuzit, "Closed-loop experimental validation of the spatially filtered Shack-Hartmann concept," *Opt. Lett.* **30**, 1255–1257 (2005).

1. Introduction

Nowadays, the field of high contrast imaging in astronomy is in great progress. Indeed, most of the large telescopes in operation are equipped with adaptive optics systems (NACO on the European Southern Observatory (ESO) Very Large Telescope (VLT) [1], Altair on Gemini North [2], Keck-AO on the Keck II telescope [3] for example. Stellar coronagraphy is also being used in combination with some of these systems [4].

Some astrophysical programmes are still out of reach with the existing instruments, due to the relatively limited performance of these systems in terms of the achieved contrast. More specifically, extra-solar planets cannot be directly detected with the current systems, except for

a few recently confirmed planetary mass companions to young brown dwarfs [5, 6, 7]. But these very favorable cases, thanks to the young age and relatively low mass of the host stars not very demanding in terms of contrast requirements, are not representative of the vast majority of the envisioned targets.

The very high contrast required for direct detection of extra-solar planets around most of the target stars, is an extremely challenging goal, for which new and dedicated instruments should be developed.

In particular, such a new instrument, called SPHERE [8, 9] is currently being developed to equip the ESO VLT by mid of 2010. SPHERE will combine eXtreme Adaptive Optics (XAO) [10], high performance coronagraphy [4] and spectroscopic and polarimetric differential imaging techniques [11, 12, 13].

For very high contrast observations, SPHERE system performance analysis has shown that the system pupil stability is one of the main limitations. The new generation of instruments will therefore need a way to very accurately control the stability of the pupil, from the telescope mirrors to the science detector, especially up to the coronagraph.

We present here our study on pupil stabilization for XAO systems, performed as part of the SPHERE phase A study. We first discuss the impact of pupil stability for extra-solar planets detection in section 2. In section 3 we present the principle of the pupil motion control and in section 4 we discuss the possible sources of errors in the measurement of the pupil shift. Finally, in section 5 we present the laboratory experiment which allowed to fully validate the proposed concept.

2. Impact of pupil motion on extra-solar planet detection

Extra-solar planet detection using ground based telescopes requires an XAO system to compensate for atmospheric turbulence and system aberrations, a coronagraphic device to cancel out the flux coming from the central star and a differential imaging technique (for instance a subtraction of two images obtained at two nearby wavelengths) to cancel out the residual un-corrected PSF pattern [11]. Limitations to this approach are mainly due to the differential aberrations in the two image channels. These differential aberrations mix up with fixed uncorrected aberrations (coming from non common path errors), leading to residual fixed patterns after image subtraction (see our simulation on figure 1). Such optical wavefront errors come from instrumental aberrations. Even if they are small, their temporal behavior is problematic due to system temporal evolution (in particular the pupil motion during the observation sequence): they are not perfectly constant and are therefore difficult to calibrate; their variability is however much too slow to be averaged with time, as with turbulence residuals.

In order to calibrate the residual pattern in differential imaging and thus to reach SPHERE required contrast of less than 10^{-6} in H band at 0.5 arcseconds, observations have to be obtained using a reference star. To be efficient, this calibration has to be performed with the whole system as stable as possible.

In particular, the telescope pupil has to remain motionless during the whole observing process, typically 1 or 2 hours. When located at the Nasmyth focus of a telescope, as SPHERE instrument will be, this stability requirement implies the use of a pupil de-rotator and a pupil re-centering device. It has been shown on simulations that a pupil shift of 1% of the pupil diameter or a pupil rotation of 1 degree will reduce by a factor of 1.5 to 2 (for typical observing conditions at the VLT) the detection capability of a coronagraphic differential imaging system.

For example, the behavior of the telescope pupil on NACO gives an order of magnitude of the pupil shift: when NACO is rotated by 180 degrees the pupil shift reaches 2% of the pupil diameter. This pupil shift is due to rotation axis misalignment, flexures of the telescope structure, M3 mirror misalignment, Nasmyth platform deformation, as well as pupil rotation

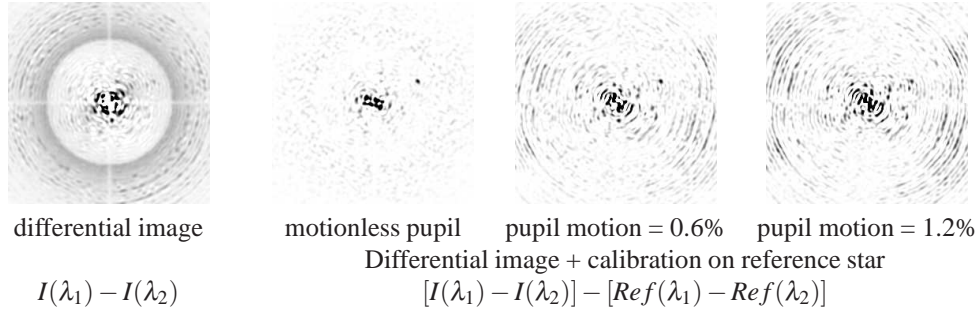


Fig. 1. [Left] Differential coronagraphic (4-quadrants) image ($\lambda_1 = 1.56\mu m$, $\lambda_2 = 1.59\mu m$), [Right] differential coronagraphic image + reference subtraction: Pupil shift between object and reference star = 0, 0.6 and 1.2 % of the full pupil. The companion ($\Delta_m = 15$, separation = 0.6 arcsec) is really distinguishable from residual fixed speckles for a fixed pupil.

errors in the case of SPHERE (non-perfect derotation system at the entrance of the SPHERE bench).

In terms of dynamical evolution, a first estimate leads to a pupil shift of 0.1% over 15 minutes. Simulations for the SPHERE have shown that the pupil stability in translation in any pupil plane must be better than 0.2% (goal 0.1%) of the pupil diameter in order to allow the detection of self-luminous young planets around solar type stars within 50 parsecs from the sun. As a typical observing sequence (science exposure followed by calibration exposure on a reference star) lasts for about an hour, a closed loop system has to be implemented in order to fulfil this tight requirement. This device will be composed of a pupil sensor and a pupil motion corrector.

3. Design of a closed-loop pupil shift corrector

The basic idea is to measure the pupil position without adding any dedicated sensor to avoid splitting the light beam and therefore wasting precious photons. Another goal was to try to keep the system as simple as possible in order to reduce its impact on the overall SPHERE instrument. Considering these two requirements we have chosen to use the existing Shack-Hartmann Wave Front Sensor (SH WFS) of the main adaptive optics loop. The only additional device will be a pupil tip-tilt mirror (PTTM) located close to the input focal plane of the instrument in order to correct for any measured pupil motion.

3.1. Principle of the sensor

The sensing principle consists in measuring the integrated flux in 4 computation areas that include sub-apertures located at the edges of the pupil (hereafter areas are labeled 1, 2, 3 and 4, see figure 2).

From the four integrated flux values (I_1, I_2, I_3 and I_4), we compute both I_x and I_y :

$$I_x = \frac{I_1 - I_3}{I_1 + I_3} \quad (1)$$

$$I_y = \frac{I_2 - I_4}{I_2 + I_4} \quad (2)$$

which give the information on pupil shifts along the x and y axes respectively.

For practical purpose, all the sub-apertures included in the four areas on figure 2 will not be used. Only sub-apertures close to the x-axis (respectively y-axis) will be included in compu-

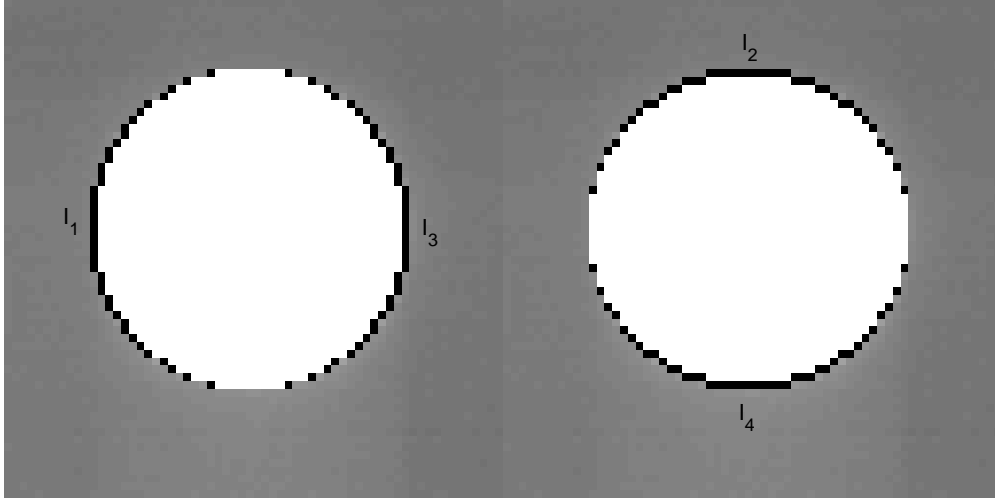


Fig. 2. Ring-shaped pattern for sub-apertures.

tation areas to measure the shift along the x -axis (respectively y -axis) because the farther the sub-apertures are from the axis the larger is the noise in the I_i signal. For example, the flux in a sub-aperture located on the y -axis does not bring any information on the shift along the x -axis, it only brings noise. Therefore, for analytical development, we will consider the pessimistic case where we use only sub-apertures close to the x and y axis. We will discuss the general case in the experimental section (see section 5).

The measurement principle is shown on figure 3 with only one sub-aperture per area. Each square in the figure represents one of the WFS sub-apertures. Hereafter, we will use the representation of this figure to develop the equations. In this case, $I_i = N \cdot S' / S$ (S and S' are defined on figure 3). Assuming that the edge of the telescope is a straight line on the computation area used to measure the pupil motion and that only sub-apertures close to the axis are used, the pupil shift amplitude d' along the x axis is directly linked to I_x by:

$$|I_x| = \frac{d'}{2 \cdot d} \quad (3)$$

where d is the sub-aperture size and $d \gg d'$ (with this approximation $I_i \propto (d - d') \cdot l$ where l is the width of the computation area). The same applies to the y axis. The sign of I_x (respectively I_y) gives the direction of the shift. We present in figure 4 the I_x signal as a function of the pupil shift. For comparison purposes, the theoretical expression of the signal (obtained for $d \gg d'$) is also plotted. One can note that linearity is maintained for shifts lower than typically 25% of a sub-aperture size.

3.2. Measurement of the integrated flux

The measurement of the integrated flux per sub-aperture must be obtained from the Shack-Hartmann spots after flat-field correction and background subtraction. In order to increase the measurement accuracy, the signal of several computation area located at the pupil edge can be combined to obtain the final I_i values, including areas next to the central obscuration in the case of an astronomical reflective telescope.

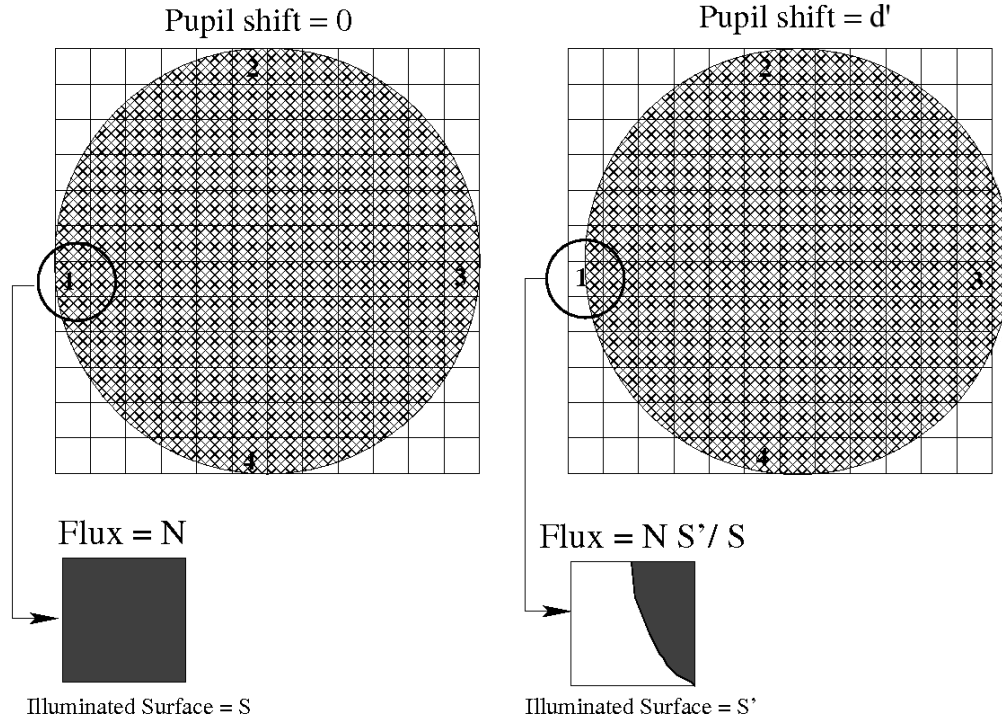


Fig. 3. Schematic representation of the pupil shift measurement using a SH WFS.

3.3. principle of the correction

We first need to measure the flux received by each sub-aperture using a calibration source (located at the entrance of the adaptive optics system) to determine reference values. Using these reference values, the pupil is roughly centered "by hand". Then, an interaction matrix is acquired using the tip-tilt mirror located in a focal plane. Next, a command matrix is computed by direct inversion of the interaction matrix. Finally, when the pupil motion correction system is running, a closed loop measurement of I_1 , I_2 , I_3 and I_4 allows to compute the corrections which are sent to the control loop of the pupil tip-tilt mirror.

4. Performance study

Before performing an experimental validation of the concept, an analytical study has been conducted. In this study, the different sources of measurement error are discussed, as well as the impact of the atmospheric turbulence.

4.1. Measurement error

4.1.1. Photon noise

From equation 1, the noise variance on the measurement signal I_x is:

$$\sigma_x^2 = \left\langle \left(\frac{I_1 - I_3}{I_1 + I_3} \right)^2 \right\rangle - \left(\left\langle \frac{I_1 - I_3}{I_1 + I_3} \right\rangle \right)^2 \quad (4)$$

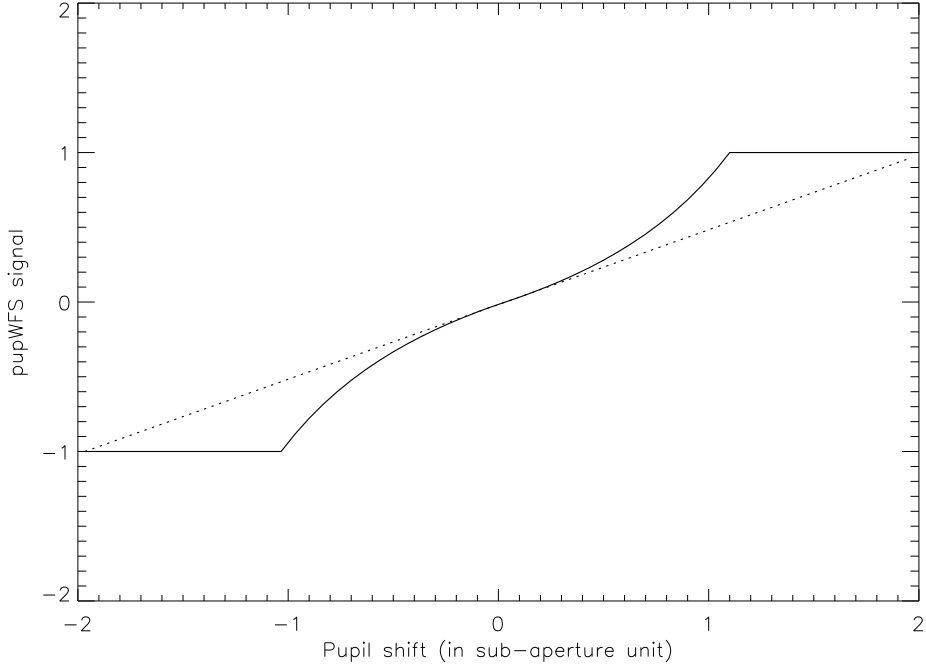


Fig. 4. I_x as a function of pupil shift (in sub-aperture unit).

Assuming that the noise fluctuations of $I_1 + I_3$ are negligible and that $I_1 + I_3 = N + N'$ with N being the number of photons in a fully illuminated area and N' the flux in the truncated area ($N' \simeq N(1 - d'/d)$ if $d' \ll d$), equation 4 becomes:

$$\sigma_{I_x}^2 = \frac{\langle I_1^2 \rangle - \langle I_1 \rangle^2 + \langle I_3^2 \rangle - \langle I_3 \rangle^2 - 2(\langle I_1 \cdot I_3 \rangle - \langle I_1 \rangle \langle I_3 \rangle)}{(N + N')^2} \quad (5)$$

Then assuming that I_1 and I_3 follow photon noise statistics and that I_1 and I_3 noises are decorrelated, it comes:

$$\sigma_{I_x}^2 = \frac{N + N'}{(N + N')^2} \quad (6)$$

and if $d \ll d'$, $N \simeq N'$, then equation 5 finally leads to:

$$\sigma_{I_x}^2 \simeq \frac{1}{2N} \quad (7)$$

Figure 5 confirms the hypothesis made to obtain equation 7. A 15×15 Shack-Hartmann has been simulated (only considering its geometry) by a flat incoming wavefront and a varying number of photons per computation area and per frame. The simulation shows that the approximations used in equation 7 are still valid up to $d' = d/2$.

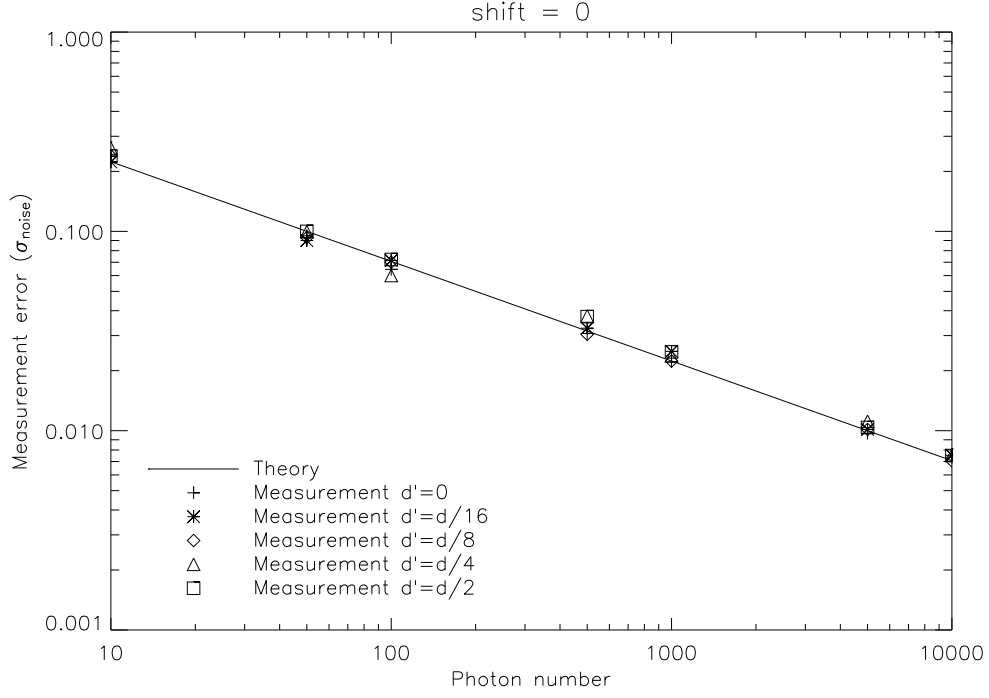


Fig. 5. Photon noise influence on pupil sensor measurement.

4.1.2. Detector noise

Following the same development as in section 4.1.1, the noise variance in the case of detector noise can be written as:

$$\sigma_{I_x}^2 \simeq \frac{2 \cdot \sigma_{detec}^2}{(N + N')^2} \quad (8)$$

where σ_{detec} is equal to $N_{pix} \times RON^2$ with N_{pix} the number of pixels per computation area and RON the detector Read-Out Noise. Again assuming $d' \ll d$, it comes:

$$\sigma_{I_x}^2 \simeq \frac{\sigma_{detec}^2}{2N^2} \quad (9)$$

4.1.3. Noise effect on pupil sensor measurement

Let us consider that the pupil sensor works in closed-loop (in term of pupil centering). In that case, the assumption that $d \ll d'$ is well verified. Then, the effects of noise (detector noise and photon noise) can be summarized in one global equation (from equations 7 and 9):

$$\sigma_{I_x}^2 \simeq \frac{N + \sigma_{detec}^2}{2N^2} \quad (10)$$

It is clear, from equation 10 that as soon as $N \gg \sigma_{detec}^2$, the dominant effect is the photon noise.

We see from equation 10 that measurement sensitivity and photons number per sub-aperture increase accordingly. For a given flux on the camera, another way to increase the sensitivity is to use a greater number of sub-apertures to measure the integrated flux in the 4 computation areas.

4.1.4. Impact of integration time on measurement noise

Assuming the following parameters

- 1e- RON CCD
- 1 kHz sampling frequency
- 6x6 pixels per sub-aperture
- Three GS magnitudes (M0 spectral type) : 9.5 (130 photons/sub-aperture/frame), 10.5 (50 photons/sub-aperture/frame), and 11.5 (20 photons/sub-aperture/frame)

one can deduce the pupil motion sensor performance as a function of the integration time. Considering that the typical evolution of the sub-aperture position is 0.1% every 15 minutes (for alt-azimuthal telescopes, it will of course depend on the zenith angle), the typical exposure time of the pupil motion sensor has to be smaller than a few minutes. In closed loop operation, the system bandwidth is typically 6 to 15 times smaller than the sampling frequency depending on the loop scheme and the overall delay. In our case, the time scale is pretty large (a few seconds to a minute) which will probably dramatically reduce the computational delay (with respect to integration time itself). It therefore seems reasonable to consider a system bandwidth equal to 1/6th of the sampling frequency. The results in Figure 6 show that the noise measurement will not be a limitation in terms of system accuracy. In any case, one can increase the number of sub-apertures (for instance all the sub-apertures located at the edge of the pupil) in order to improve the signal to noise ratio.

4.2. Impact of atmospheric turbulence

Another contribution to the flux fluctuation in each sub-aperture is the atmospheric effects which can be decomposed in two main contributors:

- the scintillation effects which induce amplitude fluctuation of the electromagnetic field during the propagation through the turbulence and thus intensity fluctuation at the level of the focal plane of each sub-aperture
- the speckle pattern in each sub-aperture PSF which randomly evolves and induces intensity fluctuations because of the finite size of the sub-aperture FoV (typically a few arcseconds).

These two effects are quantified in the following sub-sections.

4.2.1. Scintillation effect

Scintillation effects lead to sub-aperture flux variations and thus can affect the pupil motion sensor measurements. The typical size of a scintillation pattern (in the Rytov approximation,

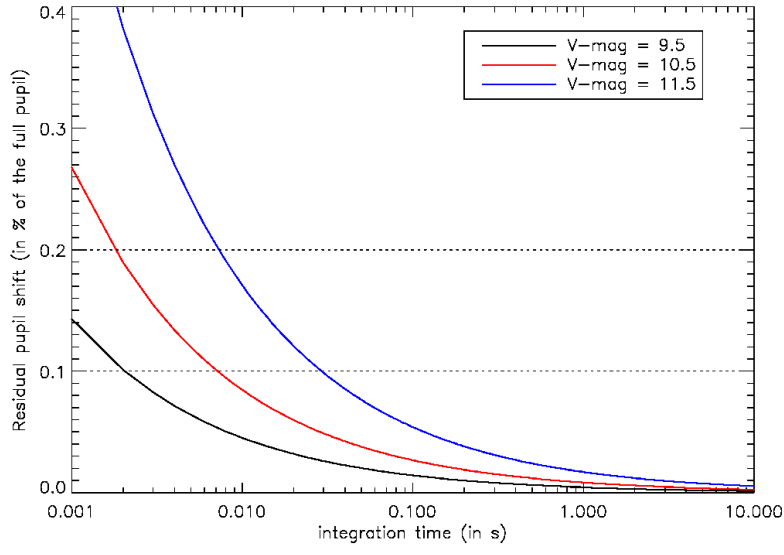


Fig. 6. Evolution of the residual pupil motion as a function of the integration time. A closed loop measurement is considered, meaning that the noise is filtered by the loop (as a function of its bandwidth: $BW = F_{samp}/6$).

well validated for astronomical observation) is given by:

$$L_{scint} = \sqrt{\lambda_{wfs} h_{eq}} \quad (11)$$

where h_{eq} represents an equivalent distance of propagation (typically a few kilometers for astronomical site). h_{eq} is given (in the Rytov approximation) by [14]:

$$h_{eq} = \left(\frac{\int_0^\infty h^2 C_n^2(h) dh}{\int_0^\infty C_n^2(h) dh} \right)^{1/2} \quad (12)$$

and λ_{wfs} the WFS wavelength. If a visible WFS is considered, $\lambda_{wfs} = 0.7 \mu m$ typically which leads to a typical size of the scintillation pattern equal to a few millimeters (4.5 millimeters for a equivalent altitude of 3 km).

In this conditions, one can assume that the scintillation patterns are by far smaller than the sub-aperture size (20 cm for the SPHERE system). Hence, the flux fluctuation per sub-aperture and per frame is given by the following expression [15]

$$\sigma_I = \sqrt{17.36 * d^{-7/3} \int_0^\infty h^2 C_n^2(h) dh} \quad (13)$$

with d the sub-aperture size and $C_n^2(h)$ the turbulence profile. For typical atmospheric condition, σ_I is equal to a few percents.

This value has to be reduced as a function of the integration time. It decreases with the factor $\sqrt{T/\tau_{scint}}$ where T is the total pupil motion sensor integration time (typical 1 min) and τ_{scint} the typical scintillation lifetime. In a first approximation, and assuming a Taylor hypothesis

$$\tau_{scint} = L_{scint}/v \quad (14)$$

with v the turbulence wind speed.

Hence, considering a 10 m/s wind speed and an integration time of typically 10 seconds (which is fast enough to correct for pupil motion at the required level of accuracy), the scintillation effects lead to flux fluctuation smaller than 0.1 % i.e. an error on pupil position of 0.005 %.

Considering the orders of magnitude involved here (especially pupil motion sensor integration time), the scintillation effects are assumed to be negligible in the global pupil motion sensor error budget.

4.2.2. Effect of sub-aperture field of view

The sub-aperture FoV leads to a flux loss (PSF turbulent wings). This flux loss evolves with the residual un-corrected turbulence and induces flux variations in the sub-aperture. We plot in Figure 7 the flux variation in one sub-aperture as a function of the FOV size. SPHERE conditions are considered here: i.e. a 0.85 arcsec seeing, a 20 cm sub-aperture size and a WFS wavelength of $0.7 \mu\text{m}$.

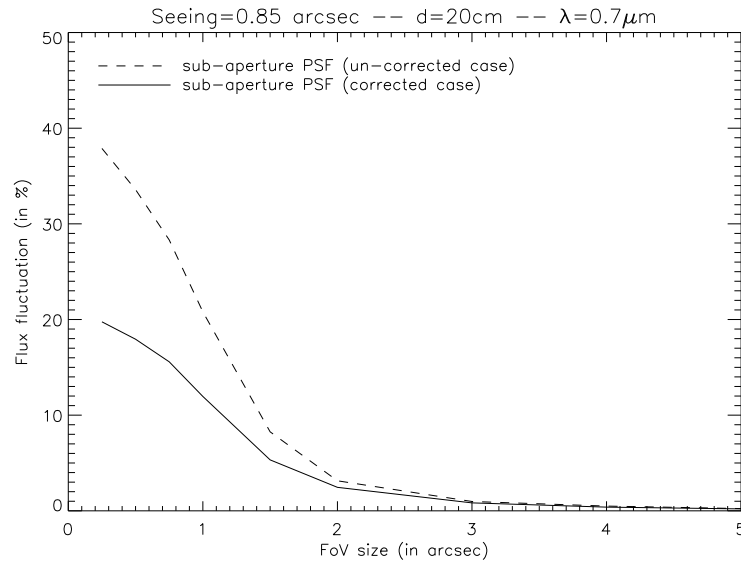


Fig. 7. Instantaneous flux fluctuation due to the sub-aperture FoV size

Figure 7 shows that for typical FoV (1 to 2 arcseconds) the instantaneous flux fluctuations are of the order of 10 to 20 % which leads to an error on pupil position between 0.5 and 1 %. As presented in the previous section for the scintillation case, this residual turbulence effect decreases with $\sqrt{T/\tau_{urb}}$ where T is the total pupil motion sensor integration time (typical 1 min) and τ_{urb} the typical residual uncorrected turbulence evolution (typical a few ms) [15, 16]. This dependency is illustrated in Figure 8 where the precision on pupil shift estimation is plotted as a function of the pupil motion sensor integration time.

Considering the orders of magnitude involved here (especially pupil motion sensor integration time), the previous analysis has shown that the residual uncorrected turbulence effects are negligible in the global pupil motion sensor error budget. In addition, one can note that the quantification presented here is probably pessimistic since the SPHERE system will integrate

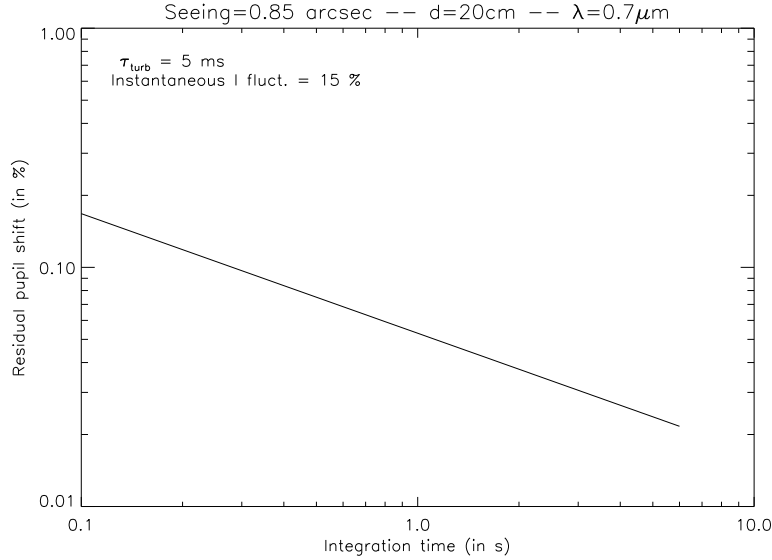


Fig. 8. Precision (in %) on pupil shift measurement as a function of pupil motion sensor integration time (only the effects of the finite FoV of the sub-apertures are considered here). $\tau_{turb} = 5ms$, seeing = 0.85 arcsec.

a spatial filter device in front of its wave front sensor [17]. This device will cancel out all the high spatial frequencies before the wave front sensor measurement. It therefore dramatically reduce the speckle pattern in each sub-aperture and leads to very clean and symmetrical spots [18].

5. First experimental validation

In order to validate our analytical study, a laboratory experiment has been elaborated.

5.1. Experimental set-up

A test bench has been installed at our laboratory to validate the pupil motion sensor concept. It is composed of a white light fiber, a pupil diaphragm, a tilt-tilt mirror located in a focal plane and a Shack-Hartmann wavefront sensor (HASO 64 from Imagine Optic). The Shack-Hartmann wavefront sensor is composed of a 64×64 micro-lens array focusing light on a DALSA CCD camera (Read Out Noise = $51e^{-2}$). We consider only a 40×40 sub-apertures illuminated disc over the 64×64 sub-apertures.

A first lens is located at a focal distance from a light source to obtain a parallel incident beam. The entrance pupil of the telescope is defined by a diaphragm, optically conjugated with the lenslet plane of the SH WFS. The Tip-Tilt Mirror (TTM) is located in a focal plane in order to control the pupil movement. The TTM actuators generate pupil shifts in the X and Y directions.

5.2. Comparison between analytical and experimental results

5.2.1. Study of the Pupil Motion Sensor response

Choice of the computation areas

Four computation areas are located at the edge of the pupil. The width of each sub-aperture

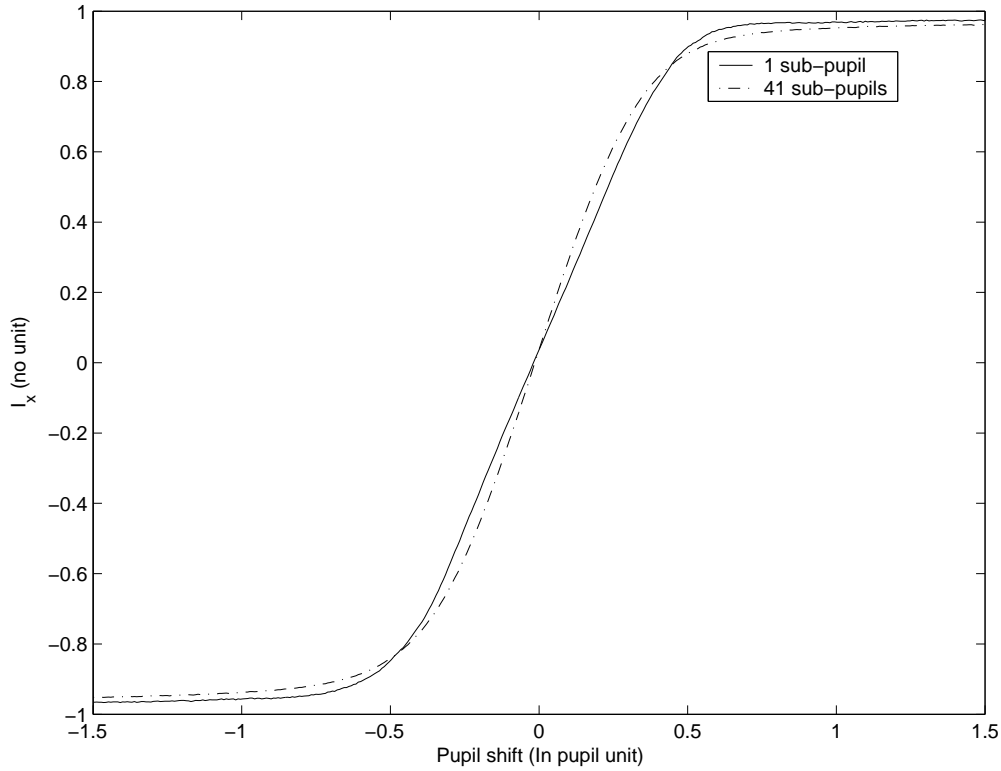


Fig. 9. Response curves for sub-apertures with 1 and 41 sub-apertures.

allows a maximum pupil shift measurement of $1/40^{th}$ pupil (i.e. 2.5% of the pupil diameter). A pattern with the maximum of sub-apertures per computation areas (41 sub-apertures surrounding the pupil at the most) is defined on figure 2. Each pixel in the figure represents the integrated flux of a SH WFS sub-aperture.

We study in the following paragraphs how the pupil measurement evolves with the number of useful sub-apertures. One can already guess that, since the integrated flux increases with the number of sub-apertures, the sensitivity of the measurement will increase accordingly as long as the selected sub-apertures are close to the corresponding axis (so the equation 3 is valid).

Response curves

We present in figure 9 the experimental signal I_x as a function of pupil shift S . The pupil shift is a linear function of the voltage V_x applied to the x-actuator of the TTM. Two curves are represented, showing two different configurations for the computation areas:

- with 4 sub-apertures (one per direction).
- with all the sub-apertures located at the edge and surrounding the telescope pupil.

Figure 9 shows that the curve slope increases when the number of sub-apertures increases meaning that the pupil motion sensor sensitivity increases with the number of sub-apertures. It is clear that the larger the number of sub-apertures (bringing information on the signal of interest) the better the measurement accuracy should be.

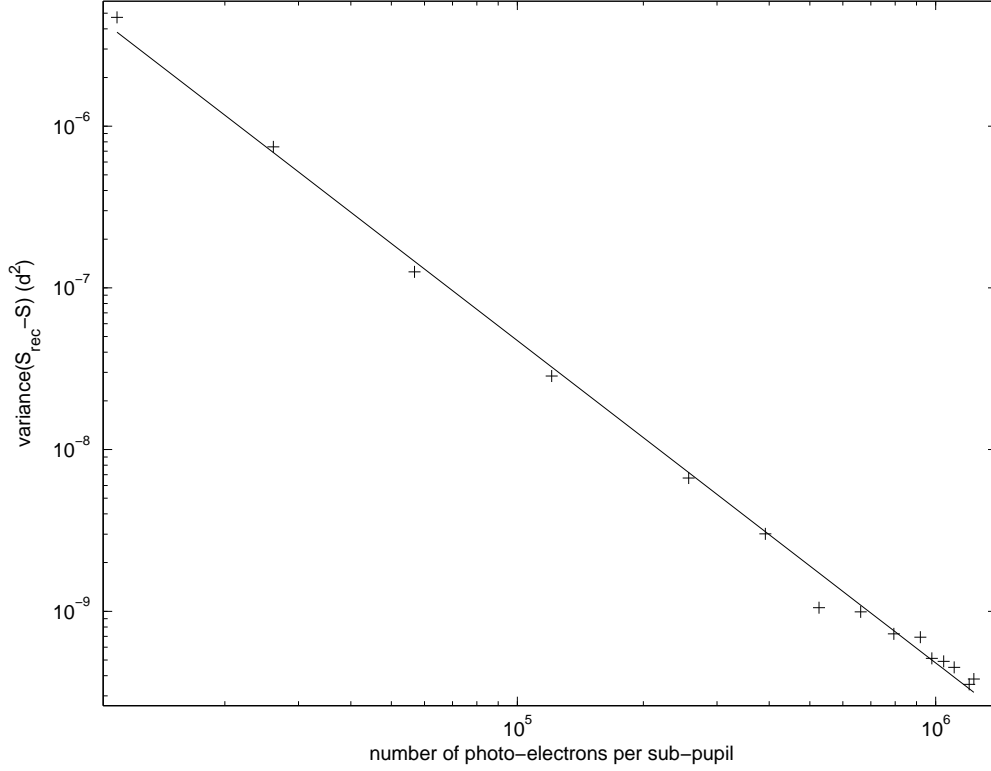


Fig. 10. Reconstruction error as a function of the number of photons with one sub-aperture.

5.2.2. Example of reconstruction

After the acquisition of an interaction matrix and a computation of a command matrix (direct inversion of the interaction matrix), pupil shift measurements (i.e. the intensity fluctuation on the considered sub-apertures, I) and their corresponding pupil shift (S_{rec}) are estimated.

In order to determine the measurement sensitivity, we plot the variance of $(S - S_{rec})$ (where S is the true pupil shift introduced by the PTTM) as a function of the number of photons received on the CCD camera as illustrated in figure 10. For example, in our case, to be able to detect a pupil shift smaller than 0.1% of the pupil diameter, the measurement error must be smaller $10^{-7}d^2$. We see that a minimum number of 7 sub-apertures located at the edge of the pupil (see figure 11) is required to fulfil the SPHERE specification for a reasonable number of photons received on the detector (about 10^5 photons per sub-apertures).

The measurement accuracy increases rapidly with the number of sub-apertures, but then saturates, typically when more than 20 sub-apertures per computation areas are used (figure 11). So it shows that it is useless to include too many sub-apertures in computation areas because the ones located far from the axis bring more noise than signal.

We can compare the measured variance with the analytical results obtained in 10. The reconstruction error is plotted in figure 10 as a function of the number of photons per sub-aperture. The effect of photon noise cannot be studied with the detector of the HASO-64 because the

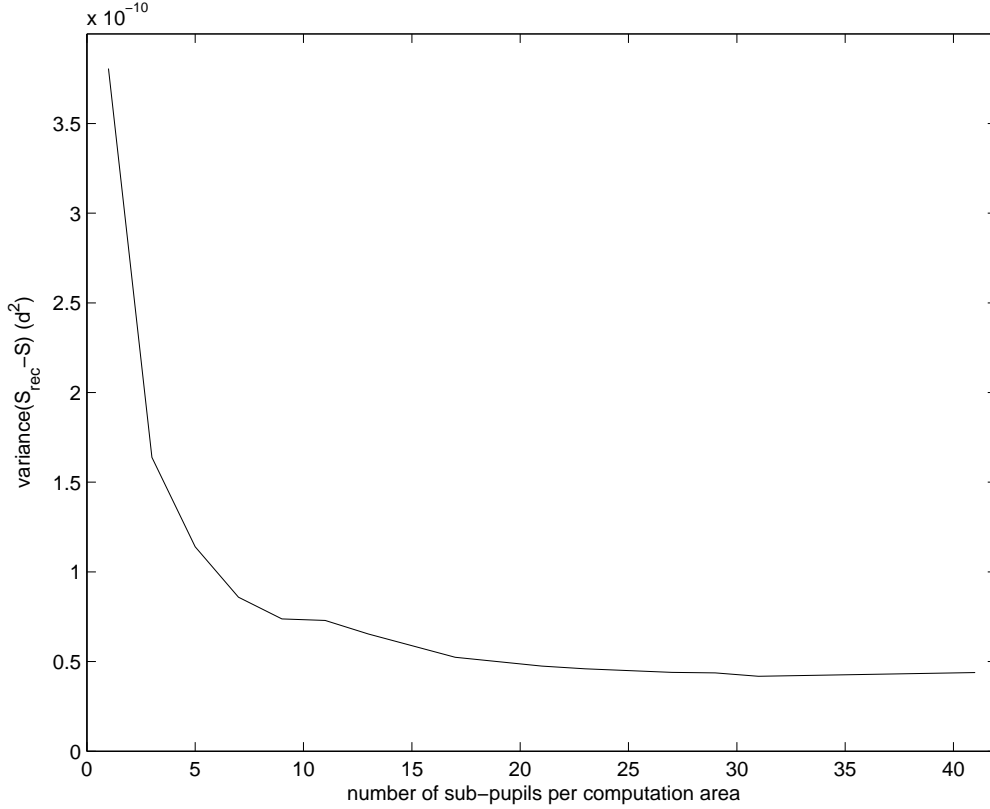


Fig. 11. Reconstruction error as a function of the number of selected sub-apertures.

CCD camera saturates before $N \simeq \sigma_{detec}^2$. Therefore, we only see here the influence of the detector noise:

$$\sigma_{I_x}^2 \propto \frac{\sigma_{detec}^2}{2N^2} \quad (15)$$

A very good agreement is found between the analytical expression and the measurements: the experimental are well fitted by the analytical equation.

6. Conclusion and perspectives

We have proposed a simple and efficient concept for pupil motion tracking and compensation during a SPHERE closed loop observation sequence. Analytical, simulation and experimental studies have been conducted to validate the concept and to quantify its performances. Each item of the error budget have been identified and quantified showing that the pupil motion sensor fullfill (with some appreciable margins) all the SPHERE requirements. In addition, a first experimental validation has shown the relative simplicity of implementation and use of the device. Furthermore, experimental results match analytical ones with a good accuracy which is very encouraging for the future overall performance of the pupil motion sensor en SPHERE.